Hybrid Sinusoidal-Pulse Charging Method for the Li-Ion Batteries in Electric Vehicle Applications Based on AC Impedance Analysis

Sideng Hu[†], Zipeng Liang[*], and Xiangning He[*]

[†,*]College of electrical engineering, Zhejiang University, Hangzhou, China

Abstract

A hybrid sinusoidal-pulse current (HSPC) charging method for the Li-ion batteries in electric vehicle applications is proposed in this paper. The HSPC charging method is based on the Li-ion battery ac-impedance spectrum analysis, while taking into account the high power requirement and system integration. The proposed HSPC method overcomes the power limitation in the sinusoidal ripple current (SRC) charging method. The charger shares the power devices in the motor inverter for hardware cost saving. Phase shifting in multiple pulse currents is employed to generate a high frequency multilevel charging current. Simulation and experimental results show that the proposed HSPC method improves the charger efficiency related to the hardware and the battery energy transfer efficiency.

Key words: Battery charger, Efficiency, Electric vehicle, Impedance

I. INTRODUCTION

Li-ion batteries are widely used in energy storage systems (ESS) owing to their high energy density, good cycle-life performance, and low self-discharge rate. Battery chargers and their corresponding charging methods are conceived as a bridge for the electricity and chemical energy transformation in ESS. They both affect the system performance [1], [2] including the charging speed, cycle life, system efficiency, etc. Many charging methods have been discussed in the literature, such as constant-current (CC) charging, constant-voltage (CV) charging [3], and pulse charging (PC). Among them, the CC and CV are the most extensively used. However, the polarization effect and diffusion limitation of distribute more uniformly. However, the effect of periodic pulse profiles on the overall performance of systems is still vague when compared with CC with the same mean current lithium ions in fast charging applications degrade their performance [4], [5]. Pulse charging (PC) provides a rest period for the ions to diffuse and for the electrolyte ions to [6], [7]. Other charging techniques are proposed to obtain better battery charging performance. These include fuzzy control, neural network, and gray prediction [8]-[10]. However, the circuit design of such charging systems is found to be complicated and expensive.

Battery chargers, as the charging executors in ESS, have also been studied extensively to achieve higher efficiency, compact structure and easy integration [11]-[13]. Numerous assessments have been carried out to improve the charger efficiency through soft switching [14], [15], auxiliary circuits [16], hybrid topology, etc. [17].

In addition to hardware efficiency, the energy transfer efficiency of a battery is also important to an ESS. The energy transfer efficiency is the ratio of the charging and discharging capacity in the electrochemical reaction cycle of a battery. Recently, a sinusoidal ripple current (SRC) charging method has been proposed as a feasible solution for better charging performance with minimum battery ac impedance Z_{min} [18], [19]. The experimental results in [18] show that, compared with the conventional CC charging method, the charging time, energy transfer efficiency, maximum rising temperature, and lifetime of the Li-ion battery in the SRC test have been improved by about 17%, 1.9%, 45.8%, and 16.1%, respectively.

However, further improvements are still required before implementing the SRC into practice. First, the generator of the high rate-high frequency sinusoid charging current lacks detail. A dual active bridge is proposed in [20] to output a

sinusoid charging current. However, the charging frequency is fixed instinctively at two times the line voltage frequency. That is not able to achieve the minimum ac impedance Z_{min} for a Li-ion battery. A sinusoid charging current of 1kHz with an average current of 1.5A is generated in [18]. However, the charger efficiency is neglected. In addition, the above method is not flexible enough to integrate with existing vehicle on-board systems. Finally, the impact of charging frequency variations of Z_{min} is not clear.

This paper focuses on improving the overall efficiency of ESSs by a combination of the minimum-ac-impedance theory in SRC and power electronics charging technology. The effectiveness of the proposed method is experimentally compared with that of the SRC, PC and CC methods.

II. AC-IMPEDANCE CHARACTERISTIC OF LI-ION BATTERIES AND ENERGY TRANSFER EFFICIENCY

Fig. 1 shows a Li-ion battery ac-impedance model. Assuming that the charging frequency is f_s, the ac impedance of the battery can be written as (1) [18], [21], and [22]:

$$Z_{battery}(2\pi f_s) = \left[R_o + \frac{\frac{R_{ct}}{(2\pi f_s C_d)^2}}{R_{ct}^2 + \left(\frac{1}{2\pi f_s C_d}\right)^2} \right] + j\left[2\pi f_s L_d - \frac{\frac{R_{ct}^2}{2\pi f_s C_d}}{R_{ct}^2 + \left(\frac{1}{2\pi f_s C_d}\right)^2} \right] \quad (1)$$

where R_{ct} is the transfer resistance, C_d represents the double layer capacitance, R_o is the ohmic resistance, and L_d is the anode inductance. The frequency f_{Zmin} that corresponds to the minimum ac impedance Z_{min} is:

$$f_{Zmin} = \frac{1}{2\pi R_{ct} C_d}\sqrt{K-1} \quad (2)$$

where:

$$K = \frac{\sqrt{2R_o R_{ct}^3 C_d^2 + 2L_d R_{ct}^2 C_d + R_{ct}^4 C_d^2}}{L_d}$$

As shown in Fig. 1, the frequency for the minimum impedance can be utilized to reduce the energy loss in the battery charging process, which leads to the maximum energy transfer efficiency (the optimal electrochemical reaction) [23]-[25]. Here, the energy transfer efficiency is expressed as:

$$n = \frac{Q_{discharge}}{Q_{charge}}$$
$$= \frac{I_{discharge} * T_{discharge}}{I_{charge} * T_{charge}} \quad (3)$$

where $Q_{discharge}/Q_{charge}$ is the discharging/charging capacity, $I_{discharge}/I_{charge}$ represents the discharging/charging current, and $T_{discharge}/T_{charge}$ means the discharging/charging time.

III. PRINCIPLE OF THE HYBRID SINUSOIDAL-PULSE CHARGING METHOD BASED ON THE AC IMPEDANCE CHARACTERISTIC

In this section, an ac impedance characteristic test for Li-ion batteries is presented. It is performed by an ac impedance analyzer CHI650E as shown in Fig. 2. To avoid the capacity
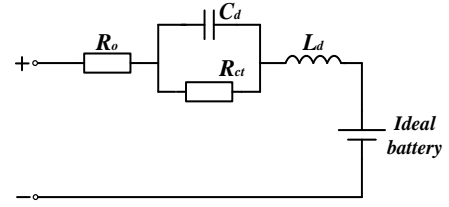

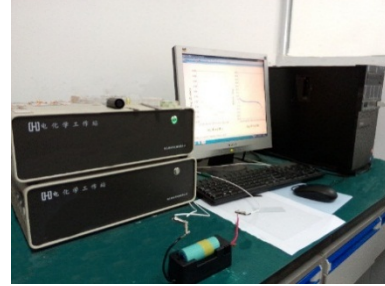Fig. 1. Li-ion battery ac impedance model.
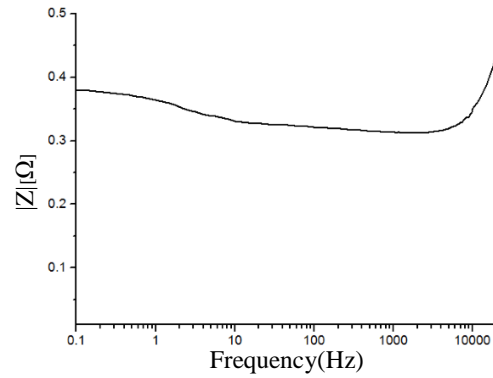

Fig. 2. Ac-impedance analyzer.

Fig. 3. Measured ac impedance spectrum of a Li-ion Battery.

TABLE I
AC IMPEDANCE RESULT BY BATTERY-CHARGING TEST

Frequency [Hz]	500	1000	2000	2300	5000	10000
$|Z|[\Omega]$	0.319	0.318	0.317	0.316	0.320	0.350

error caused by the activation effect of a virgin li-ion battery, the test battery is extracted from a cycled battery package. Fig. 3 shows the ac-impedance spectrum test results. Some data are presented in TABLE I, where the minimum-ac-impedance frequency f_{Zmin} and the minimum ac impedance Z_{min} are 2.3kHz and 0.316Ω, respectively.

As shown in Fig. 3, the curve of $|Z_{battery}|$ is flat within the frequency domain where Z_{min} exist. The $|Z_{battery}|$ varies within 1.5% from $f_{Zmin}/4$ to $4f_{Zmin}$. Therefore, multiple currents with frequencies around f_{Zmin} can also be utilized to achieve the energy transfer efficiency improvement, due to the impendence reduction.

A multilevel current source is used for the multiple frequencies charging the current generation, as shown in Fig. 4. It is composed of three parallel boost circuits. The

inductors L_1, L_2, and L_3 can be inductors or motor stator windings. Based on the experimental tests and data in [18], a frequency range of 3-5 kHz matches the traction application switching frequencies. This implies the HSPC generator can share the switches in a three phase traction inverter. The device S_1, S_2, and S_3 are the switching devices in the lower bridge arm of a three phase inverter, and D_1, D_2, and D_3 utilize the anti-parallel diode of the upper bridge arm. In forming three boost converters, the dc source voltage must be less than the battery package voltage on the board.

In Fig. 5 the duty cycle of any output current i_{Dx} in one boost unit is 1-D, where D represents the duty cycle for S_x, assuming a continuous inductor current. For the symmetrical distribution of i_{Dx} in i_{ch}, the time shift between i_{D1} and i_{D2} is Δt_{12} and is equal to $\frac{1}{3}DT_s$. The time shift between i_{D1} and i_{D3} is Δt_{13} and is equal to $\frac{2}{3}DT_s$. Since $0 < \Delta t_{12} < \Delta t_{13} < (1-D)T_s$, the duty cycle limit can be deduced as D<0.6.

Fig. 5 shows the operation of a circuit with D=½. u_{g1}-u_{g3} are the driving signals for the switches S_1-S_3. i_{D1}-i_{D3} are the currents through diodes D_1-D_3. The switches S_2, and S_3 have a phase shift of 360°×½×⅓=60° and 360°×½×⅔=120° to S_1, respectively. There are six sequential operation modes in one cycle, as shown in Fig. 6.

Mode 1[t_0-t_1]: Switches S_1 and S_2 are in the on-state, and S_3 is turned on at t_0. L_1-S_1, L_2-S_2, and L_3-S_3 conduct current, as shown in Fig. 6(a). The battery charging current i_{ch} is zero.

Mode 2[t_1-t_2]: At t_1, switch S_1 is turned off, and the current in S_1 flows through L_1-D_1 to charge the battery. The battery charging current is the same as the current through L_1, as shown in Fig. 6(b).

Mode 3[t_2-t_3]: At t_2, switch S_2 is turned off. L_1-D_1, L_2-D_2, and L_3-S_3 conduct current. As shown in Fig. 6(c), the battery charging current is the sum of the currents in L_1 and L_2.

Mode 4[t_3-t_4]: At t_3, switch S_3 is turned off. L_1-D_1, L_2-D_2, and L_3-D_3 conduct current. As shown in Fig. 6(d), the charging current is the sum of the currents in L_1, L_2 and L_3.

Mode 5[t_4-t_5]: At t_4, switch S_1 is turned on. As shown in Fig. 6(e), which is similar to mode 3, the battery charging current is the sum of the currents in L_2 and L_3.

Mode 6[t_5-t_6]: At t_5, switch S_2 is turned on. As shown in Fig. 6(f), which is similar to mode 3, the battery charging current is equivalent to the current in L_3.

Then, the system returns to mode 1 to start a new cycle. The switching frequency of each bridge device is equal to the desired charging frequency, that is, f_{Zmin}.

Fig. 6 shows that with a phase-shifting of 60°, the output forms a multilevel charging current similar to the voltage from a multilevel voltage inverter. The switch operates in a chopping mode which is different from the constant current region operation in [18]. Therefore, the power loss in a device can be reduced. The duty cycle and switching frequency of
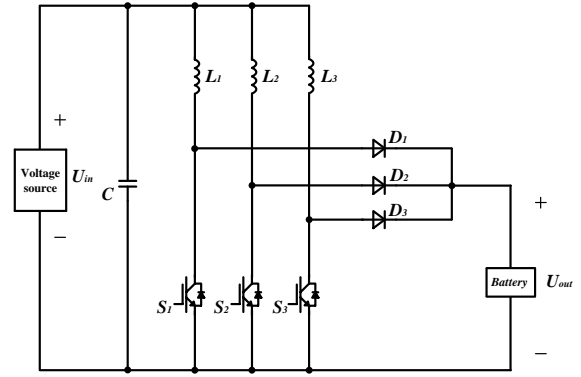

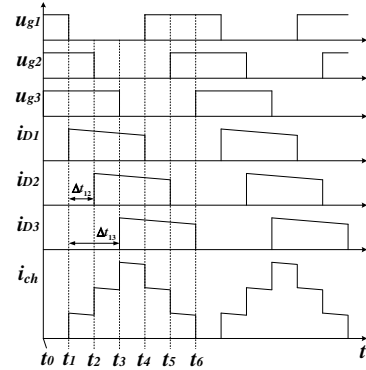Fig. 4. Schematic of proposed charging circuit.

Fig. 5. Waveform of driving signal and current.

each boost leg is adjusted to regulate the charging current. The proposed circuit can be extended to an N phase topology with multiple inductors or windings, like a multi-phase motor. Then switch S_{i+1} has a phase delay of $\frac{2\pi}{N}D$ compared to switch S_i, $1 \le i \le N$. The PC charging method can also be performed with a zero phase delay.

IV. SYSTEM DESIGN AND CONTROL SCHEME

As mentioned in section III, the devices in HSPC can be shared with the switching devices and the anti-parallel diode in three phase traction inverters. Here, the inductance value in the system design is discussed based on the output current waveform analysis.

The output current waveform i_{Dx} in one boost unit is shown in Fig. 7, using i_{D2} as an example. When S_2 is turned off, the D_2 current is equal to the inductor current, with an average I_L. The current ripple of i_{D2} is expressed in (4). Thus, the actual diode D_2 current from $-\frac{T_s}{2}(1-D)$ to $\frac{T_s}{2}(1-D)$ can be obtained by (5):

$$\Delta i_{D_2} = \frac{V_{in}DT_s}{2L} \tag{4}$$

$$i_{D_2}(t) = I_L - \frac{V_{in}D}{(1-D)L}t \tag{5}$$

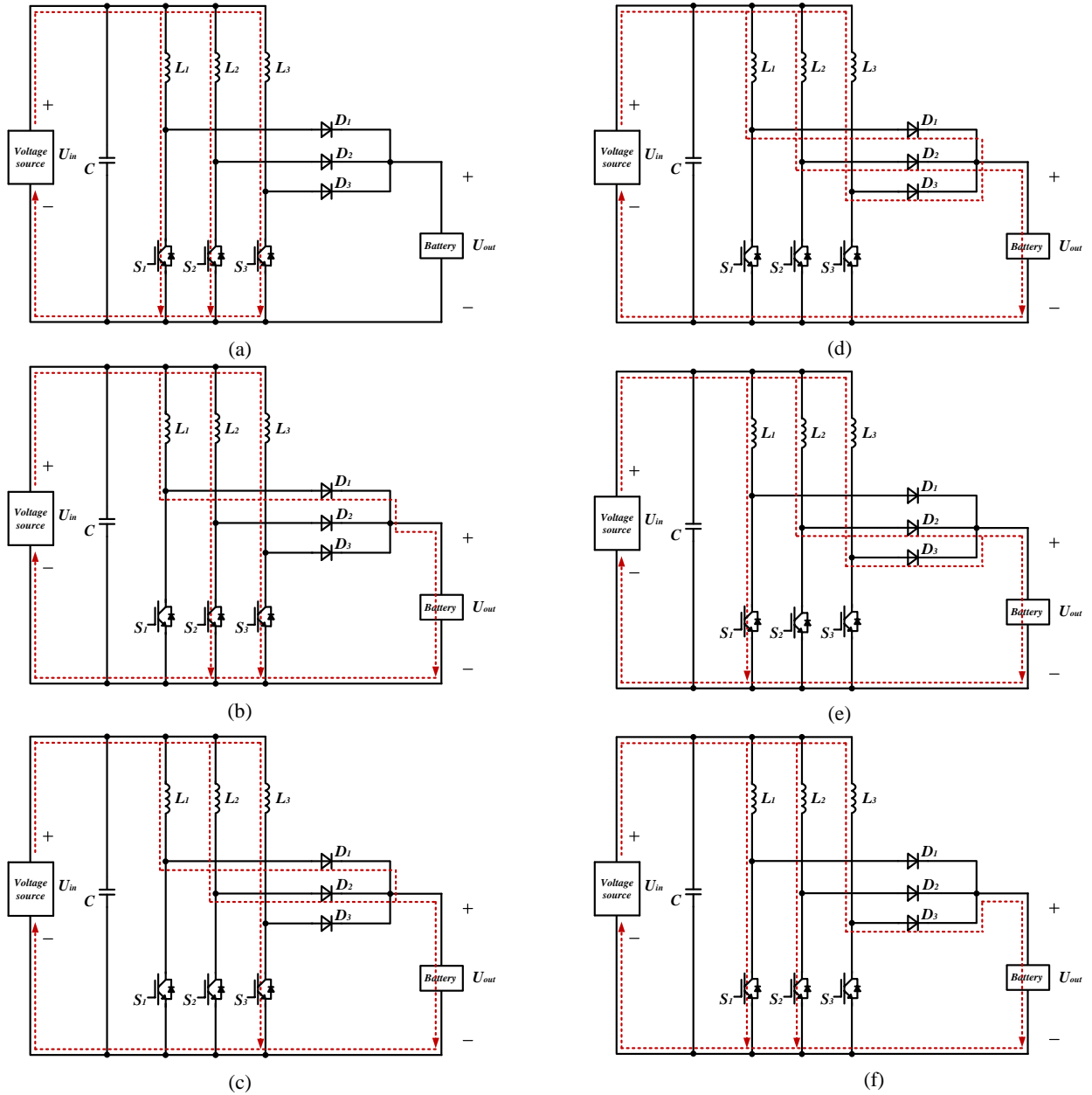where V_{in} is the input voltage and L is the inductance value of

Fig. 6. Operation modes of the proposed battery charging circuit.

L_2. The fundamental component of i_{D2} can be derived as $i_\omega(t)$ in (6):

$$i_\omega(t) = a_1 \cos \omega t + b_1 \sin \omega t \tag{6}$$

$$a_1 = \frac{2}{T_s} \int_{-\frac{1}{2}(1-D)T_s}^{\frac{1}{2}(1-D)T} i_{D_2} \cos(\omega t) dt$$
$$= \frac{2I_L}{\pi} \sin(1-D)\pi \tag{7}$$

$$b_1 = \frac{2}{T_s} \int_{\frac{1}{2}(1-D)T_s}^{\frac{1}{2}(1-D)T} i_{D_2} \sin(\omega t) dt$$
$$= \frac{1}{\pi} \frac{V_{in} D T_s}{L} \left[\cos(1-D)\pi - \frac{1}{(1-D)\pi} \sin(1-D)\pi \right] \tag{8}$$

Since i_{D1} and i_{D3} have phase shifts of $-\frac{2}{3}\pi D$ and $\frac{2}{3}\pi D$ with respect to i_{D2}, the fundamental wave total charging current is as equation (9):

$$I_\omega(t) = \left(1 + 2\cos\frac{2}{3}\pi D\right)\left(a_1 \cos\omega t + b_1 \sin\omega t\right) \tag{9}$$

From (7-9), b_1 is more complicated than a_1 for the fundamental wave estimation. In fact, a_1 presents the fundamental component of I_L in (5), and b_1 presents the fundamental component of Δi_{D2} in (5), which is smaller than a_1. Thus, to achieve a better fundamental wave estimation, L need to be designed to decrease b_1 in (9). A close loop based on (7) is demonstrated in Fig. 8.

In Fig. 8, the average current regulator can be an ac/dc or dc/dc converter to perform the current regulation and electric isolation. v_{in} can be regulated by the PI controller of I_L in the current regulator voltage loop. The system command I_L^*
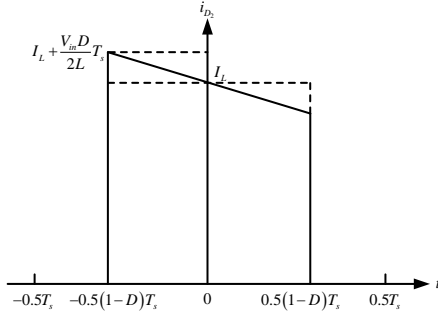
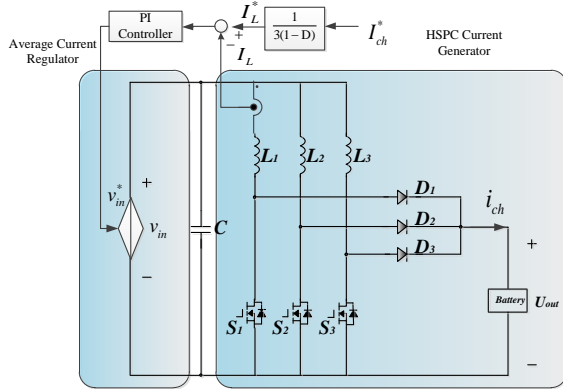Fig. 7. Analysis of the output current i_{Dx} in one boost unit.

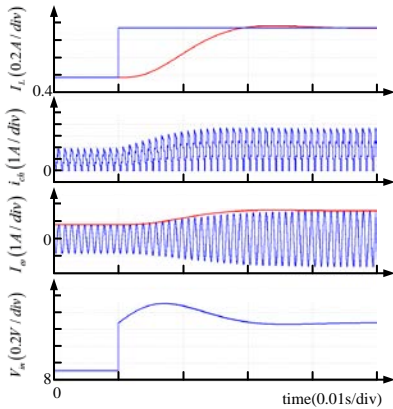Fig. 8. Control scheme of proposed system.

Fig. 9. Close-loop control performance (simulation).

is calculated by the average charge current command I_{ch}^* :

$$I_L^* = \frac{I_{ch}^*}{3(1-D)} \qquad (10)$$

The HSPC generator aims at charging current shaping through duty cycle D adjustment. The relationship between the current total harmonic distortion (THD) in HSPC and D is analyzed in the Appendix. The effectiveness of the control method above is demonstrated in Fig. 9.

The average inductor current I_L follows the system command through V_{in} well. The peak value estimation in (9) is well matched with the envelope of I_ω in the charging current, and the fundamental charging current estimation is verified.
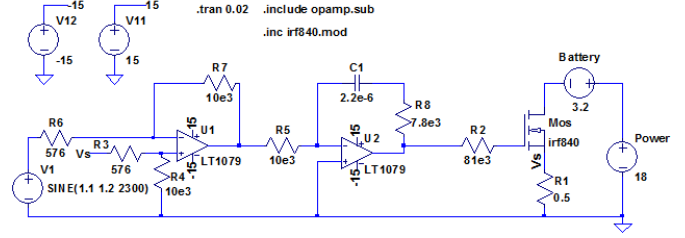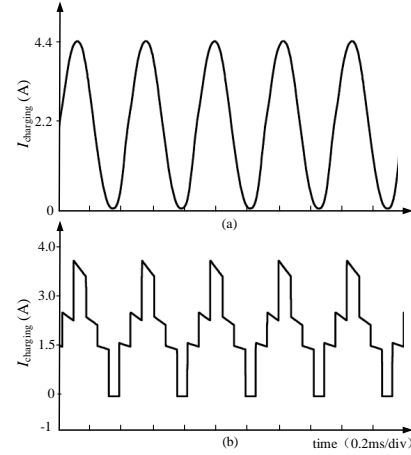

Fig. 10. Schematic of SRC charging circuit.

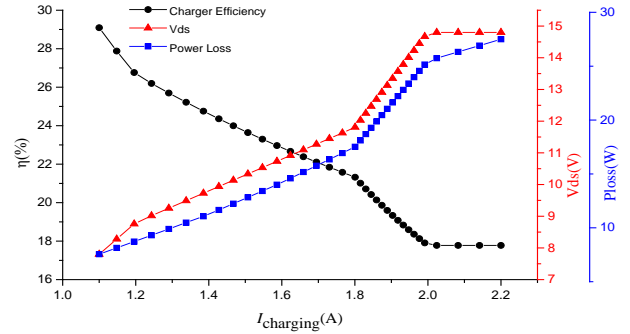Fig. 11. Simulation waveform of the charging current in SRC (a) and (b) HSPC.

Fig. 12. Power loss and Vds on MOSFET with different average currents.

V. CHARGER EFFICIENCY COMPARISON

As discussed in previous sections, the charging efficiency is defined by the charger efficiency and the energy transfer efficiency. In this section, the charger efficiencies of HSPC and SRC are compared.

First, the SRC and HSPC charging methods are assessed by LTSPICE to get the power loss without a heat sink or cooling system. The schematic of the SRC charger and its closed-loop control circuit is shown in Fig. 10.

As shown in Fig. 10, a dc voltage source is selected as the battery load and a MOSFET IRF840 is used, which enables the reference to the switching device and experimental test in [18]. The spice IRF840 model was provided by the device manufacturer. The current peak-peak value is 4.4A and the

average is 2.2A as shown in Fig. 11. The output current is 2.3kHz and the power loss in the device increases with a increasing output current, as shown in Fig. 12.

The results in Fig. 12 are calculated according to (11):

$$
\begin{aligned}
\eta &= \frac{P_{battery}}{P_{battery} + P_{R1} + P_{MOS}} \\
&= \frac{I_{ch}E_{battery}}{I_{ch}(E_{battery} + V_{R1} + V_{ds})} \\
&\approx \frac{E_{battery}}{E_{battery} + V_{ds}} \\
&= \frac{1}{1 + \dfrac{V_{ds}}{E_{battery}}}
\end{aligned}
\tag{11}
$$

where I_{ch} is the average value of the charging current, V_{R1} is the voltage in the current sampling resistor R_1, V_{ds} is the MOSFET voltage, and $E_{battery}$ is the battery terminal voltage. As shown in (11), the efficiency is dominated by the ratio between V_{ds} and $E_{battery}$. $E_{battery}$ rises slightly following the charging current, while V_{ds} increases significantly due to the constant current region requirement. Thus, the power loss increased significantly with the charging current, as shown in Fig. 12. The power loss increment is 20W when the charging current increases from 0.5C to 1C, during which the charger efficiency falls from 30% to 17%.

The power loss on the device of the HSPC is calculated with the same average current and switching devices, as shown in Fig. 13. Only the MOSFET power loss is considered while the losses in the inductor and diode are not included. The square symbol means the power loss in a single MOSFET while the circle symbol represents the charger efficiency including three MOSFETs. The power loss is much smaller when compared with Fig. 12. The efficiency varies from 79% to 90% depending on the charging current.

Next, the output current harmonic characteristic of the HSPC is compared with the SRC and pulse current (PC) charging methods. The PC duty ratio is 50% and the frequency is the same as for the HSPC.

The FFT results of both output currents are shown in Fig. 14. The average current is the same but the harmonics of the PC over 10kHz are much higher than the HSPC. The RMS currents of the PC, SRC and HSPC are 3.11A, 2.69A and 2.57A, respectively. Therefore, the power loss in R_0 caused by the pulse is 1.46 times that of the HSPC, causing an additional temperature rise.

VI. ENERGY TRANSFER EFFICIENCY COMPARISON

In this section the energy transfer efficiency is tested experimentally for the HSPC, PC, SRC and CC.

Fig. 15 shows the battery-charging energy transfer test platform that comprises battery test equipment, an SRC
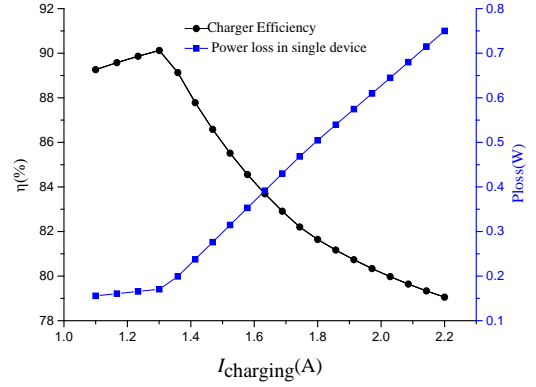

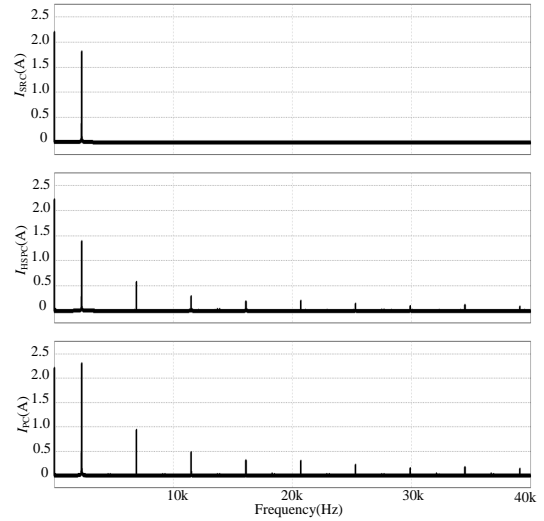Fig. 13. Power loss in switching device with different charging current value.

Fig. 14. FFT analysis of the charging current in SRC, HSPC and PC.
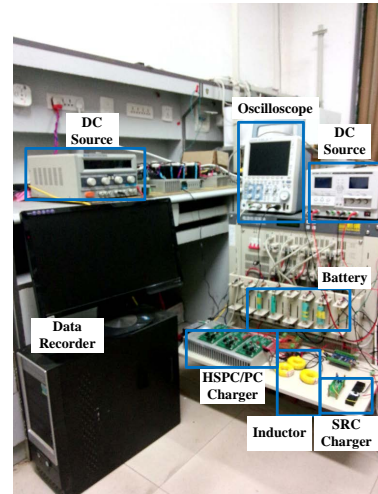

Fig. 15. Battery test platform.

charger, and a charger that can perform the HSPC and PC functions. The inductors L_1, L_2, and L_3 are manufactured with different values, i.e. 2.5mH, 2.4mH, and 4mH, for inductance variation consideration in the motor windings. The battery
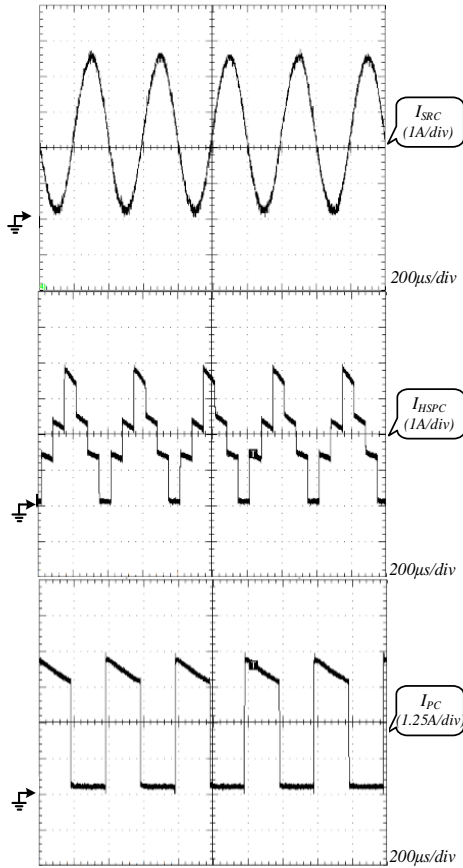
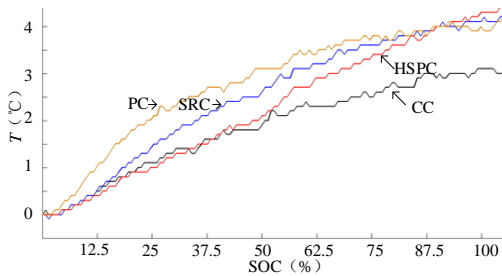Fig. 16. Charging current waveform of SRC, HSPC and PC.

Fig. 17. Temperature rising comparison of four charging method.

test equipment can perform CC charge method, and the temperature rising for all four of the tests is saved to a data recorder. The charging frequency of the HSPC, PC and SRC are all set in 2.3kHz. The average current is 2.2A. Fig. 16 shows the generated SRC, HSPC and PC charging currents, and all of the tests are carried on the same battery.

Fig. 16 shows the results from the HSPC and SRC methods. The charger can output HSPC current under the asymmetric bridges inductance situation. The temperature rising and charging efficiency are shown in Fig. 17 and Fig. 18. The temperature rising in Fig. 17 shows that the CC has the minimum charging temperature rising. The rise in the SRC and HSPC are similar. The PC has the maximum temperature rising, which corresponds to the charging current RMS calculation in section V.
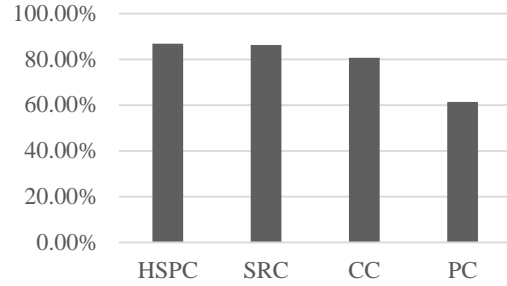

Fig. 18. Energy transfer efficiency comparison.

Fig.18 compares the energy transfer efficiency of the four charging methods. The proposed HSPC and the SRC have the best performance in energy transfer efficiency, while the PC has the lowest efficiency.

VII. CONCLUSION

In this paper, a hybrid sinusoidal-pulse-current charging method (HSPC) was proposed and tested for the Li-ion batteries in electric vehicle applications. The proposed topology consisted of three parallel connected boost circuits. This method is based on the ac-impedance spectrum and aims at high power requirements and vehicle power train system integration. The proposed method was compared with the SRC, PC and CC methods. It was established that the charger efficiency and energy transfer efficiency in a battery can be improved with the HSPC, resulting in a higher system level efficiency. The application of this method can be extended to other battery types, for example, lead-acid batteries.

APPENDIX

The THD analysis of the HSPC current is derived based on the charging current in Fig. 5:

$$i_{ch}(t) = \begin{cases} 0 & 0 \le t < \frac{1}{3}DT_s \\ I_L & \frac{1}{3}DT_s \le t < \frac{2}{3}DT_s \\ 2I_L & \frac{2}{3}DT_s \le t < DT_s \\ 3I_L & DT_s \le t < 1-\frac{2}{3}DT_s \\ 2I_L & 1-\frac{2}{3}DT_s \le t < 1-\frac{1}{3}DT_s \\ I_L & 1-\frac{1}{3}DT_s \le t \le T_s \end{cases} \quad (12)$$

In section IV, the average charging current and fundamental wave have been derived by equation (13) and (14), respectively. The root-mean-square value of the charging current is derived as (15).

$$I_{ch} = 3(1-D)I_L \quad (13)$$

$$I_\omega(t) \approx \left(1 + 2\cos\frac{2}{3}\pi D\right) a_1 \cos \omega t$$
$$= \left(1 + 2\cos\frac{2}{3}\pi D\right) \cdot \frac{2I_L}{\pi}\sin(1-D)\pi \cos \omega t \quad (14)$$
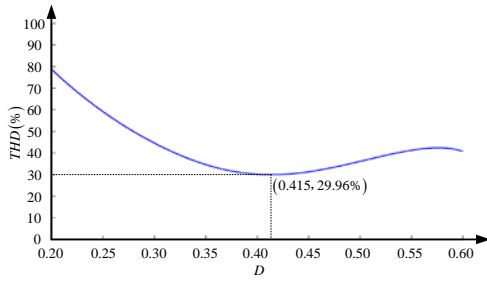
Fig. 19. The relationship of THD and D.

$$I_{ch\_rms} = \sqrt{9 - \frac{35}{3}D}\, I_L \qquad (15)$$

Based on equations (13)-(15), the THD of the charging current is calculated in equation (16):

$$\text{THD} = \sqrt{\frac{I_{ch\_rms}^2 - I_L^2 - \left(I_\omega / \sqrt{2}\right)^2}{\left(I_\omega / \sqrt{2}\right)^2}}$$

$$= \sqrt{\frac{\frac{1}{3}\left(19D - 27D^2\right) - \frac{2}{\pi^2}\left(1 + 2\cos\frac{2}{3}\pi D\right)^2 \sin^2(1-D)\pi}{\frac{2}{\pi^2}\left(1 + 2\cos\frac{2}{3}\pi D\right)^2 \sin^2(1-D)\pi}} \qquad (16)$$

It is implied in equation (16) that the THD of the charging current depends only on the duty cycle as shown in Fig. 19:

The minimum THD is 30% in Fig. 19, when the duty cycle is 0.415. The curve is flat at around 0.415, and D can be selected in that region, when the device current and voltage stress are considered.

ACKNOWLEDGMENT

REFERENCES

[1] F. T. Siang and W. T. Chee, "A review of energy sources and energy management system in electric vehicles," *Renewable and Sustainable Energy Reviews*, Vol. 20, pp. 82-102, Apr. 2013.

[2] C. Xiang, Y. Wang, S. Hu, and W. Wang, "A new topology and control method for a hybrid Battery-Ultracapacitor energy storage system," *Energies*, Vol. 7, No. 5, pp. 2874-2896, Apr. 2014.

[3] B.-Y. Chen and Y.-S. Lai, "New digital-controlled technique for battery charger with constant current and voltage control without current feedback," *IEEE Trans. Ind. Electron.*, Vol. 59, No.3, pp. 1545-1553, Mar. 2012.

[4] H. J. Chiu, L.-W. Lin, P.-L. Pan, and M.-H. Tseng, "A novel rapid charger for lead-acid batteries with energy recovery," *IEEE Trans. Power Electron.*, Vol. 21, No. 3, pp. 640-647, May 2006.

[5] B. Dickinson and J. Gill, "Issues and benefits with fast charging industrial batteries," in *Proc. 15th Battery Conf. on Appl. and Advan.*, pp. 223-229, Jan. 2000.

[6] F. Savoye, P. Venet, M. Millet, and J. Groot, "Impact of periodic current pulses on Li-ion battery performance," *IEEE Trans. Ind. Electron.*, Vol. 59, No. 9, pp. 3481-3488, Sep. 2012.

[7] Z. Jiang and R. A. Dougal, "Synergetic control of power converters for pulse current charging of advanced batteries from a fuel cell power source," *IEEE Trans. Power Electron.*, Vol. 19, No. 4, pp. 1140-1150, Jul. 2004.

[8] G.-C. Hsieh, L.-R. Chen, and K.-S. Huang, "Fuzzy-controlled Li-ion battery charge system with active state-of-charge controller," *IEEE Trans. Ind. Electron.*, Vol. 48, No. 3, pp. 585-593, Jun. 2001.

[9] Y.-H. Liu, J.-H. Teng, and Y.-C. Lin, "Search for an optimal rapid charging pattern for lithium-ion batteries using ant colony system algorithm," *IEEE Trans. Ind. Electron.*, Vol. 52, No. 5, pp. 1328-1336, Oct. 2005.

[10] L.-R. Chen, R. C. Hsu, and C.-S. Liu, "A design of grey-predicted Li-ion battery charge system," *IEEE Trans. Ind. Electron.*, Vol. 55, No. 10, pp. 3692-3701, Oct. 2008.

[11] A. Khaligh and S. Dusmez, "Comprehensive topological analysis of conductive and inductive charging solutions for PHEV," *IEEE Trans. Veh. Technol.*, Vol. 61, No. 8, pp. 3475-3489, Oct. 2012.

[12] D. S. Gautam, F. Musavi, M. Edington, W. Eberle, and W. G. Dunford, "An automotive onboard 3.3 kW battery charger for PHEV application," *IEEE Trans. Veh. Technol.*, Vol. 61, No. 8, pp. 3466-3474, Oct. 2012.

[13] H. Bai and C. Mi, "Comparison and evaluation of different DC/DC topologies for plug-in hybrid electric vehicle chargers," *International Journal of Power Electronics*, Vol. 4, No. 2, pp. 119-133, Feb. 2012.

[14] Y.-C. Chuang, "High-efficiency ZCS buck converter for rechargeable batteries," *IEEE Trans. Ind. Electron.*, Vol. 57, No. 7, pp. 2463-2472, Jul. 2010.

[15] B. Gu, J.-S. Lai, N. Kees, and C. Zheng, "Hybrid-switching full-bridge DC-DC converter with minimal voltage stress of bridge rectifier, reduced circulating losses, and filter requirement for electric vehicle battery chargers," *IEEE Trans. Power Electron.*, Vol. 28, No.3, pp. 1132-1144, Mar. 2013.

[16] S. Hu, J. Deng, C. Mi, and M. Zhang, "Optimal design of line level control resonant converters in plug-in hybrid electric vehicle battery chargers," *IET Electrical Systems in Transportation*, Vol. 4, No.1, pp. 21-28, Mar. 2014.

[17] B. Gu, C. Lin, B. Chen, J. Dominic, C. Zheng, and J. Lai, "A high efficiency hybrid resonant PWM zero-voltage-switching full-bridge DC-DC converter for electric vehicle battery chargers," in *Proc. 28th IEEE APEC Conf.*, pp. 23-30, Mar. 2013.

[18] L.-R. Chen, S.-L. Wu, D.-T. Shieh, and T.-R. Chen, "Sinusoidal-Ripple-Current charging method and optimal charging frequency study for Li-ion batteries," *IEEE Trans. Ind. Electron.*, Vol. 60, No.1, pp. 88-97, Jan. 2013.

[19] L.-R. Chen, J.-J. Chen, C.-M. Ho, S.-L. Wu, and D.-T. Shieh, "Improvement of Li-ion battery discharging performance by pulse and sinusoidal current strategies," *IEEE Trans. Ind. Electron.*, Vol. 60, No. 12, pp. 5620-5628, Dec. 2013.

[20] L. Xue, D. Diaz, Z. Shen, F. Luo, P. Mattavelli, and D. Boroyevich, "Dual active bridge based battery charger for plug-in hybrid electric vehicle with charging current containing low frequency ripple," in *Proc. 28th IEEE APEC Conf.*, pp. 1920-1925, Mar. 2013.

[21] S. Rodrigues, N. Munichandraiah and A. K. Shukla, "AC impedance and state-of-charge analysis of a sealed

lithium-ion rechargeable battery," *Journal of Solid State Electrochemistry*, Vol. 3, pp. 397-405, Feb. 1999.

[22] K. Amine, C. H. Chen, J. Liu, M. Hammond, A. Jansen, D. Dees, I. Bloom, D. Vissers, and G. Henriksen, "Factors responsible for impedance rise in high power lithium ion batteries," *Journal of Power Sources*, Vol. 97-98, pp. 684-687. Jul. 2001.

[23] L.-R. Chen, C.-M. Young, N.-Y. Chu, and C.-S. Liu, "Phase locked bidirectional converter with pulse charge function for 42-V/14-V dual-voltage PowerNet," *IEEE Trans. Ind. Electron.*, Vol. 58, No. 5, pp. 2045-2048, May 2011.

[24] R. M. Spotniz, "AC impedance simulation for lithium-ion cells," in *Proc. 15th Battery Conf. on Appl. and Advan.*, pp. 121-126, 2000.

[25] D. Qu, "The AC impedance studies for porous MnO_2 cathode by means of modified transmission line model," *Journal of Power Sources*, Vol. 102, No. 1-2, pp. 270-276, Dec. 2001.

Sideng Hu was born in China, in 1984. He received his Ph.D. degree from Tsinghua University, Beijing, China, in 2011. From August 2011 to August 2013, he was a Post-doctoral Researcher with the University of Michigan, Dearborn, MI, USA. Since September 2013, he has been with the College of Electrical Engineering, Zhejiang University, Hangzhou, China. His current research interests include high-frequency dc/dc converters, soft-switching techniques, and vehicle electrification.

Zipeng Liang was born in China, in 1992. He received his B.S. degree from Zhejiang University, Hangzhou, China, in 2015. Since July 2015, he has been working towards his Ph.D. degree in the College of Electrical Engineering, Zhejiang University. His current research interests include power converters, renewable energy, and vehicle electrification.

Xiangning He was born in China, in 1961. He received his B.S. and M.S. degrees from the Nanjing University of Aeronautical and Astronautically, Nanjing, China, in 1982 and 1985, respectively; and his Ph.D. degree from Zhejiang University, Hangzhou, China, in 1989. Since 1996, he has been a Full Professor in the College of Electrical Engineering, Zhejiang University. Dr. He is a Fellow of The Institute of Electrical and Electronics Engineers (IEEE) and was appointed as an IEEE Distinguished Lecturer by the IEEE Power Electronics Society in 2011. He is also a Fellow of the Institution of Engineering and Technology (formerly IEE), U.K.